Research
AI Energizes Process Manufacturing—Article

A Cell Condition-Sensitive Frequency Segmentation Method Based on the Sub-Band Instantaneous Energy Spectrum of Aluminum Electrolysis Cell Voltage

Zhaohui Zeng [a,b], Weihua Gui [a], Xiaofang Chen [a,*], Yongfang Xie [a], Hongliang Zhang [c], Yubo Sun [a]

[a] School of Automation, Central South University, Changsha 410083, China
[b] Key Laboratory of Intelligent Computing & Information Processing, Ministry of Education, Xiangtan University, Xiangtan 411105, China
[c] School of Metallurgy and Environment, Central South University, Changsha 410083, China

A B S T R A C T

Cell voltage is a widely used signal that can be measured online from an industrial aluminum electrolysis cell. A variety of parameters for the analysis and control of industrial cells are calculated using the cell voltage. In this paper, the frequency segmentation of cell voltage is used as the basis for designing filters to obtain these parameters. Based on the qualitative analysis of the cell voltage, the sub-band instantaneous energy spectrum (SIEP) is first proposed, which is then used to quantitatively represent the characteristics of the designated frequency bands of the cell voltage under various cell conditions. Ultimately, a cell condition-sensitive frequency segmentation method is given. The proposed frequency segmentation method divides the effective frequency band into the [0, 0.001] Hz band of low-frequency signals and the [0.001, 0.050] Hz band of low-frequency noise, and subdivides the low-frequency noise into the [0.001, 0.010] Hz band of metal pad abnormal rolling and the [0.01, 0.05] Hz band of sub-low-frequency noise. Compared with the instantaneous energy spectrum based on empirical mode decomposition, the SIEP more finely represents the law of energy change with time in any designated frequency band within the effective frequency band of the cell voltage. The proposed frequency segmentation method is more sensitive to cell condition changes and can obtain more elaborate details of online cell condition information, thus providing a more reliable and accurate online basis for cell condition monitoring and control decisions.

© 2021 THE AUTHORS. Published by Elsevier LTD on behalf of Chinese Academy of Engineering and Higher Education Press Limited Company. This is an open access article under the CC BY-NC-ND license (http://creativecommons.org/licenses/by-nc-nd/4.0/).

1. Introduction

Cell voltage is an important signal that can be measured online and is widely used in industrial aluminum electrolysis cell control systems. The filtered voltage, smoothed voltage, voltage slope, voltage swing, and voltage vibration calculated with the cell voltage are essential parameters for cell control systems, enabling such systems to control the alumina concentration [1–3], cell temperature [4], and cell stability, and to analyze the cell condition [5–7]. Although it is time-series data with a simple structure, the cell voltage contains a wealth of cell condition information of different frequencies, including status information, such as the alumina concentration [8–11]; external interference information caused by mechanical actions or manual operations; and internal environmental change information caused by molten aluminum rolling (metal pad rolling (MPR)), line current oscillations (COs), anode gas emissions, anode faults, and so forth [10,12]. This cell condition information of different frequencies is often superimposed together and eventually appears as various complex oscillation forms in the cell voltage. The low-frequency component of the cell voltage corresponding to the alumina concentration is used to calculate the voltage slope [2,13,14]; the low-frequency noise of the cell voltage related to the metal (molten aluminum) movement is used to calculate the voltage swing; and the high-frequency noise of the cell voltage that is linked to anode problems is used to calculate the voltage vibration [15,16]. Cell voltage frequency segmentation is the basis for determining the passband of digital filters that are used to separate the cell voltage components

---

* Corresponding author.
  E-mail address: xiaofangchen@csu.edu.cn (X. Chen).

relating to these pieces of cell condition information [17]. Therefore, proper cell voltage frequency segmentation is conducive to obtaining more accurate online parameters and can thus provide a reliable online basis for cell condition analysis and control decisions.

In the filtering algorithms used in Refs. [1,18], the filter passbands are determined by means of experience and field experiments. Therefore, the accuracy of the parameters is affected by the relative arbitrariness. Related investigations from the frequency domain are relatively rare. In Refs. [10,11], fast Fourier transform is used to analyze the cell voltage of the 160 and 350 kA industrial cells, and frequency segmentation methods are obtained. The fast-Fourier-transform-based method loses the appearance time of the frequency of interest and is prone to generating pseudo-spectral peaks, which affect the accuracy of the cell voltage frequency segmentation. Based on empirical mode decomposition (EMD) and the Hilbert transform [19,20], the instantaneous energy spectrum based on empirical mode decomposition (EMD-IEP or EIEP) is obtained by decomposing the signal into several intrinsic mode functions (IMFs) and then calculating the Hilbert amplitude square of each IMF. The EMD determines the IMFs according to the envelopes defined by the local maxima and minima of the analyzed signal, which are greatly affected by the characteristics of the analyzed signal; thus, EMD does not perform well in the analysis of different signals with common properties. Therefore, the EIEP has a limited ability to express the commonness of different signals with common properties, and it is difficult to reflect the energy change of the components in a designated frequency band. Because the cell voltage is very complicated, especially under certain abnormal cell conditions, oscillation is more frequent. Therefore, the EIEP is not suitable for the investigation of cell voltage frequency segmentation.

The wavelet transform provides a time–frequency analysis method for complex non-stationary time series through multi-resolution analysis [21]. The scalogram provides a method to visually display the signal energy distribution on the time–frequency plane [22–25], and research using the scalogram for cell voltage frequency segmentation is rare. To analyze the characteristics of the cell voltage energy distribution corresponding to a variety of representative cell conditions in a visual manner, this paper combines the scalogram and mechanism knowledge to link the characteristics of the frequency change, the time when the frequency change occurs, and the cause of the frequency change. Then, a sub-band instantaneous energy spectrum (SIEP) based on the Hilbert transform and integral wavelet transform is proposed, through which the energy distribution in the designated frequency band of the cell voltage is quantized to obtain the sensitive frequency band of each cell condition. Finally, the frequency segmentation is guided by the cell condition-sensitive frequency band, and a method for segmenting the frequency of cell voltages is presented.

2. Qualitative analysis of the energy distribution of normalized cell voltage (NCV) under various cell conditions

The cell voltage is composed of the anode voltage, cathode voltage, counter electromotive force, electrolyte voltage, and external voltage. In the anode voltage, the greatest influencing factor is the film voltage, π_{film}, caused by the film resistance. Based on experiments and theoretical analysis, such as laboratory experiments and thermodynamic calculations, it is known that the cell voltage is affected by multiple factors such as the alumina concentration, anode–cathode distance, anode bubbles, cell temperature, electrolyte composition, and current density. These factors all change in real time with the cell conditions and are difficult to

measure online in real time. When some cell conditions appear, the associated factors become the dominant factors, and then the cell voltage shows the resulting specific forms. Therefore, from the perspective of the process mechanism, analyzing the correspondence between different cell conditions and cell voltage forms can provide a more accurate and detailed basis for the frequency segmentation of the cell voltage.

Usually, a pseudo cell resistance is used instead of the sampling cell resistance as the main basis for cell condition analysis and process control because the sampling cell resistance changes with the line current and the cell resistance does not theoretically follow the line current change. Therefore, using the pseudo cell resistance as the main basis can eliminate the interference caused by changes in the line current. The pseudo cell resistance $R_0(k)$ (where k is the sampling time) is calculated by a sampling cell voltage (SCV) $U(k)$ and a sampling line current $I(k)$ according to Eq. (1).

$$R_0(k) = \frac{U(k) - B}{I(k)} \tag{1}$$

where B is the pseudo counter electromotive force, which is generally a constant. Because the unit of voltage (mV or V) is more intuitive in industrial production, in most practical control systems, the cell resistance is linearly transformed into the "NCV" with the same meaning, that is

$$U_0(k) = R_0(k)I_b + B = \frac{U(k) - B}{I(k)}I_b + B \tag{2}$$

where $U_0(k)$ is the NCV at time k and I_b is the basic line current.

NCVs U1, U2, U3, and U4 are taken as examples to analyze and discuss the time–frequency characteristics of the NCV under various cell conditions, such as the normal cell condition (NCD), after metal tapping (AMT) operation, prior to anode effect (PAE), and COs. U1, U2, U3, and U4 are NCVs with a sampling frequency of 0.1 Hz (effective frequency band: [0, 0.05] Hz) from a 400 kA cell.

2.1. Property analysis of NCV under NCD

A time–frequency analysis of U1 (Fig. 1(a)) under NCD is conducted in this subsection. When collecting U1, the cell condition is normal [2,12,14]: There are no routine operations, such as metal tapping, anode change, or beam raising; no special operations, such as edge processing; and no special cell conditions, such as the anode effect. Fig. 1(b) provides the scalogram in the effective frequency band of [0, 0.05] Hz, and Fig. 1(c) shows the enlarged scalogram for [0, 0.015] Hz. Fig. 1 reveals the following information:

(1) In the entire effective frequency band of [0, 0.05] Hz, the energy gradually decreases from a low frequency to a high frequency. In the frequency band of [0, 0.01] Hz, the energy is higher.

(2) In the frequency band of [0, 0.001] Hz, there is a continuous energy region throughout the entire duration of the analysis.

(3) Unlike the energy distribution in the [0, 0.001] Hz frequency band, the energy in the [0.001, 0.010] Hz frequency band is not continuous but is concentrated in four different regions.

(4) The energy in the [0.01, 0.05] Hz band is significantly lower than that in the [0, 0.01] Hz band, and the energy distribution is significantly different from those in the [0, 0.001] and [0.001, 0.010] Hz energy bands.

According to the above analysis, in the effective frequency band, the energy of U1 is mainly distributed in the frequency band of [0, 0.01] Hz; the frequency bands of [0, 0.001], [0.001, 0.010], and [0.01, 0.05] Hz have completely different energy distribution forms.
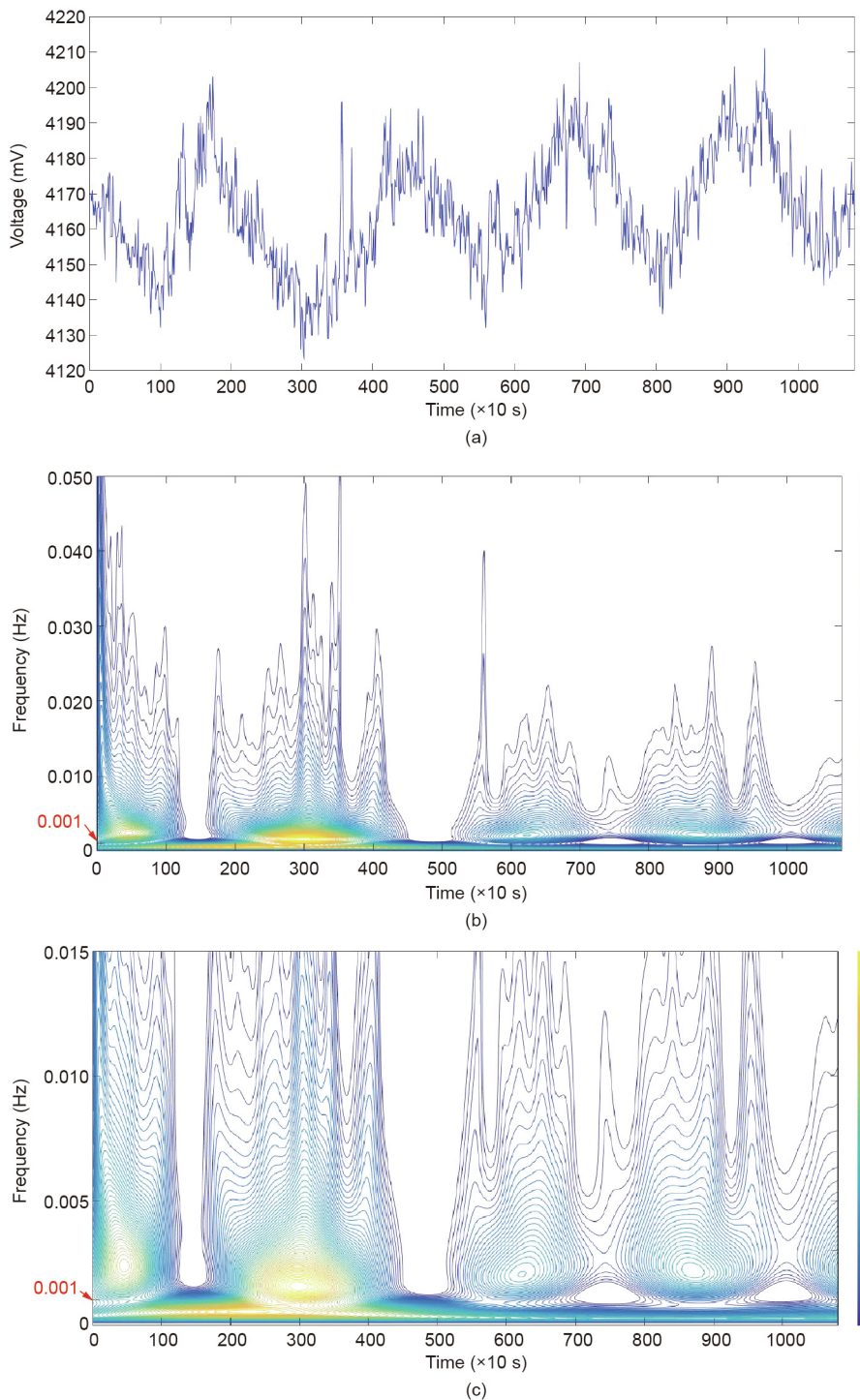
Fig. 1. Time–frequency analysis of U1 under NCD. (a) U1; (b) scalogram for [0, 0.05] Hz; (c) scalogram for [0, 0.015] Hz. The color of the color column is from dark to light, indicating the energy from weak to strong. The 0.001 Hz is the key frequency point of the frequency segmentation in this paper.

2.2. Other representative cell conditions

MPR is of great significance to the stability and current efficiency of the aluminum electrolytic production process. Different scholars have proposed various theories regarding the mechanism of MPR. Among them, the gravity wave theory [26] proposes that external disturbances will generate a gravity wave. If there is no magnetic field, the energy of the gravity wave gradually decreases and eventually disappears. If an electromagnetic field exists, the electromagnetic force will excite the existing gravity wave and generate a new gravity wave. The coupling of the electromagnetic force and the gravity wave will eventually cause a metal–bath interface wave. Ref. [27] describes the relationship among the horizontal current, magnetic field perturbation, and wave of the metal–bath interface. In Refs. [28,29], shallow water models are established to describe the magnetic–hydro–dynamic (MHD) theory of melts (metal and bath). According to MHD theory, a metal is simultaneously affected by the driving force of

electromagnetism and the reaction force of fluid gravity and viscosity resistance. Under normal conditions, these two forces achieve equilibrium, and the metal steadily rolls at a certain horizontal velocity and with a certain vertical distortion.

As shown in Fig. 2, regions i–vi represent the anode, the bath and bubble mixed layer, the bath layer, the metal–bath interface wave layer, the metal layer, and the carbon cathode, respectively. In general, the region consisting of ii, iii, and iv is called the anode–cathode distance (ACD). The metal layer (region v) and the carbon cathode (region vi) are regarded as the cathode. At present, the ACD of industrial cells is generally controlled between 40–50 mm, and Ref. [30] reports that MPR in traditional cells ranges between 9 and 15 mm. At different points in a cell, the ACD is different [31]. The change in ACD caused by MPR will be directly reflected in the cell voltage. Under normal conditions, the cell voltage oscillation is within a small range, usually between 15 and 30 mV [32].

When certain external interferences or internal environmental changes occur, the metal rolls abnormally, the metal–bath interface seriously waves, and the stability breaks down. At this time, the ACD change intensifies, and the oscillations and waves of the cell voltage appear in a special form. Because the cell is a closed system with high temperature and high corrosion, it is difficult to directly observe and measure metal pad abnormal rolling (MPAR). Usually, MPAR is inferred based on production experience and other abnormal phenomena that occur in an industrial cell. Therefore, to better design a digital filter that can separate the components related to MPAR from the NCV, it is necessary to study the frequency band of the cell voltage involved in MPAR.

2.2.1. NCV prior to the anode effect

Haupin [33] found that the average thickness of an anode bubble is 5 mm, the instantaneous thickness can reach 20 mm, and the additional voltage caused by the increase in the gas film resistance ranges between 150 and 350 mV. In addition, the behaviors of bubbles—such as sliding at the bottom of the anode, upward movement of the sides, and detachment at the edge of the anode—can cause fluctuations in the metal–bath melt. Ref. [34] reports that the wettability of the anode played a significant role in the rising behavior of the bubbles: Under an anode with poor wettability, the bubbles adhered to the anode sidewall, and there were always gas–liquid–solid three-phase contact surfaces. Prior to the anode effect, the wettability of the carbon anode under which the anode effect occurs will decrease. Therefore, the current is redistributed because the gas film resistance of the anode with poorer wettability is greater than that with better wettability. The uneven distribution of the anode current causes the horizontal
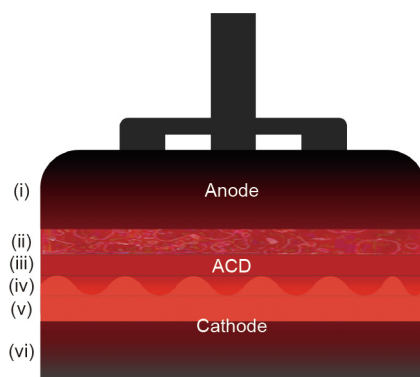
current in melts to increase, which leads to a series change of the "electric–magnetic-flow" and subsequently intensifies the melt fluctuation. By measuring and analyzing the equidistant voltage drop of the anode rod, Li et al. [35] observed that the fluctuation amplitude of the metal prior to the anode effect increased and that the fluctuation energy increased significantly. Therefore, prior to the anode effect, the real-time ACD abnormal change caused by MPAR and the increase in the gas film resistance jointly lead to an abnormal energy change of the NCV.

Fig. 3 shows NCV U2 (Fig. 3(a)) and its scalogram (Fig. 3(b)). An anode effect occurs 60 s after NCV U2. Fig. 3(b) shows that the energy distribution of U2 is basically similar to that of U1 in the frequency band below 0.01 Hz. The difference is that in the frequency band below 0.01 Hz, the energy of the last two energy accumulation regions is significantly higher than that of the first two. The closer to the occurrence of the anode effect, the more MPR in the cell intensifies, which is reflected in the significant energy increase of the corresponding moment in the U2 scalogram.

2.2.2. NCV AMT

Fig. 4 shows NCV U3 and its scalogram, from which similar conclusions to those drawn for U1 and U2 are obtained, except that the energy of the first four energy accumulation regions in the frequency band of [0.001, 0.010] Hz gradually decreases with time. This finding corresponds to the phenomenon in which the MPAR caused by the metal tapping operation gradually weakens over time [36]. Similar conclusions can be made after a time–frequency analysis of a large number of other NCVs, which were all collected AMT operations. Therefore, the following inferences can be made: ① The NCV includes information jointly introduced by the metal tapping operation and the resulting MPAR; ② this information is mainly contained in the [0.001, 0.010] Hz frequency band; and ③ after the metal tapping operation is completed, the gradual weakening of the energy in the energy accumulation zone reflects the change in the MPAR as it gradually becomes steady and gentle.

2.2.3. NCV during violent COs

Fig. 5 includes the sampling line current I4, NCV U4, the SCV U4′, and their scalograms, where the labels (X:) represent the abscissa values. Fig. 5(a) shows the I4 corresponding to U4; in Fig. 5(b), the red curve is U4, and the yellow curve is U4′ corresponding to U4; Fig. 5(c) is the scalogram of U4′; and Fig. 5(d) is the scalogram of U4. From the scalogram of U4, in the frequency bands of [0, 0.001] and [0.001, 0.010] Hz, similar conclusions to those drawn for U1, U2, and U3 are obtained. The energy distributions of U4 and U4′ in [0.01, 0.05] Hz are significantly different from those of U1, U2, and U3. The specific analysis is as follows:

(1) In Fig. 5(b), the oscillation of U4′ is significantly more severe than that of U4, especially in the period when the line current I4 (Fig. 5(a)) is oscillating significantly. The scalograms in Figs. 5(c) and (d) show that the energy of U4′ is significantly higher than that of U4 in the periods of violent COs at 2000–2500, 4000–4500, and 5000–6500 s. This result shows that the impact of COs on the cell voltage can be effectively eliminated by Eq. (2).

(2) Comparing Fig. 1(b) and Fig. 5(d), it can be seen that the energy of U4 in [0.01, 0.05] Hz is significantly higher than that of U1.

(3) The labels in Figs. 5(a), (b), and (d) show that in the periods when the line current oscillates violently, the corresponding NCVs do not have significant oscillations in the time domain. However, the scalogram in Fig. 5(d) shows that energy remains, which is mainly distributed in the frequency band of [0.01, 0.05] Hz.

According to the above analysis, Eq. (2) can effectively eliminate the violent oscillation of the cell voltage when the line current violently oscillates in the time domain, but the energy generated by the noise introduced in the frequency domain still exists. It can
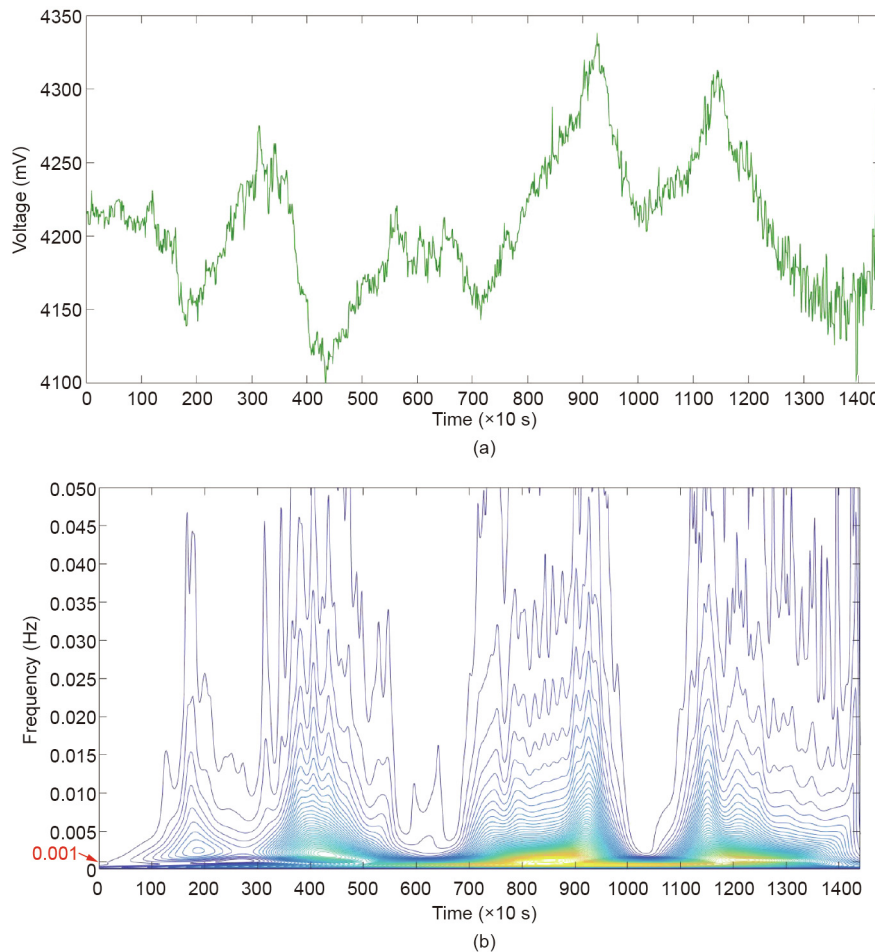

Fig. 2. Schematic diagram of the anode–cathode distance (ACD). (i) Anode; (ii) bath and bubble mixed layer; (iii) bath layer; (iv) metal–bath interface wave layer; (v) metal layer; (vi) carbon cathode.

Fig. 3. Time–frequency analysis of U2 prior to the anode effect. (a) U2; (b) scalogram of U2. The color of the color column is from dark to light, indicating the energy from weak to strong.

be inferred that the corresponding frequency band of the noise introduced by the violent oscillation of the line current is [0.01, 0.05] Hz.

2.3. Summary of the qualitative analysis on NCV

From the above analysis of the time–frequency properties of the NCVs U1–U4, the following is known:

(1) The energy of the NCV has a significantly different distribution in the three frequency bands of [0, 0.001], [0.001, 0.010], and [0.01, 0.05] Hz.

(2) The energy distribution in the [0.001, 0.010] Hz band of the NCV can reflect the MPAR caused by the metal tapping operation and anode effect. Therefore, it can be preliminarily presumed that the component of the NCV in the [0.001, 0.010] Hz band is related to the MPAR.

(3) The occurrence time of the energy abnormality of the NCV in the frequency band of [0.01, 0.05] Hz is consistent with that of the line current abnormal oscillation. It can be concluded that the violent oscillations of the line currents mainly correspond with the component of the NCV in the [0.01, 0.05] Hz band.

3. Quantitative representation of the energy change of the NCV based on SIEP

In Section 2, a qualitative analysis of the energy distribution of NCVs under various cell conditions was performed based on

mechanism knowledge and the scalogram. Based on the significantly different characteristics of the energy distribution, the effective frequency band of the NCV was initially divided into three sub-bands: [0, 0.001], [0.001, 0.010], and [0.01, 0.05] Hz. To better analyze the relation between the energy distribution of the NCV in each sub-band and the various cell conditions, such as MPAR and violent CO, this section defines the SIEP and uses it to give a quantitative representation of the energy changes in each sub-band of U1–U4.

3.1. Definition of the SIEP

Let $h_g(x)$ be the Hilbert transform of the non-stationary signal $g(x)$, where $x \in \mathbb{R}$, $\mathbb{R}$ is the real number set; then the integral wavelet transform of $h_g(x)$ is $W_g(b,a) = |a|^{-\frac{1}{2}} \int h_g(x) \cdot \overline{\psi(\frac{x-b}{a})} \cdot \mathrm{d}x$, where $a, b \in \mathbb{R}$, $a \neq 0$; $\psi \in L^2(\mathbb{R})$(where $L^2(\cdot)$ is a square integrable function), $2\pi \int |\xi|^{-1} |\widehat{\psi}(\xi)|^2 \mathrm{d}\xi < \infty$, $\widehat{\psi}$ is the Fourier transform of ψ, ξ is the frequency variable. Define the SIEP $P_{g|_{\omega_1}^{\omega_2}}$ of frequency band $[\omega_1, \omega_2]$ as follows:

$$P_{g|_{\omega_1}^{\omega_2}}(t) = \int_{\omega_1}^{\omega_2} |W_g(t,f)|^2 \cdot \mathrm{d}f \tag{3}$$

where t is the time and f is the frequency.

Eq. (3) shows that the SIEP is the time marginal distribution of the energy in frequency band $[\omega_1, \omega_2]$ of the integral wavelet transform of $h_g(x)$. The SIEP quantitatively represents the energy
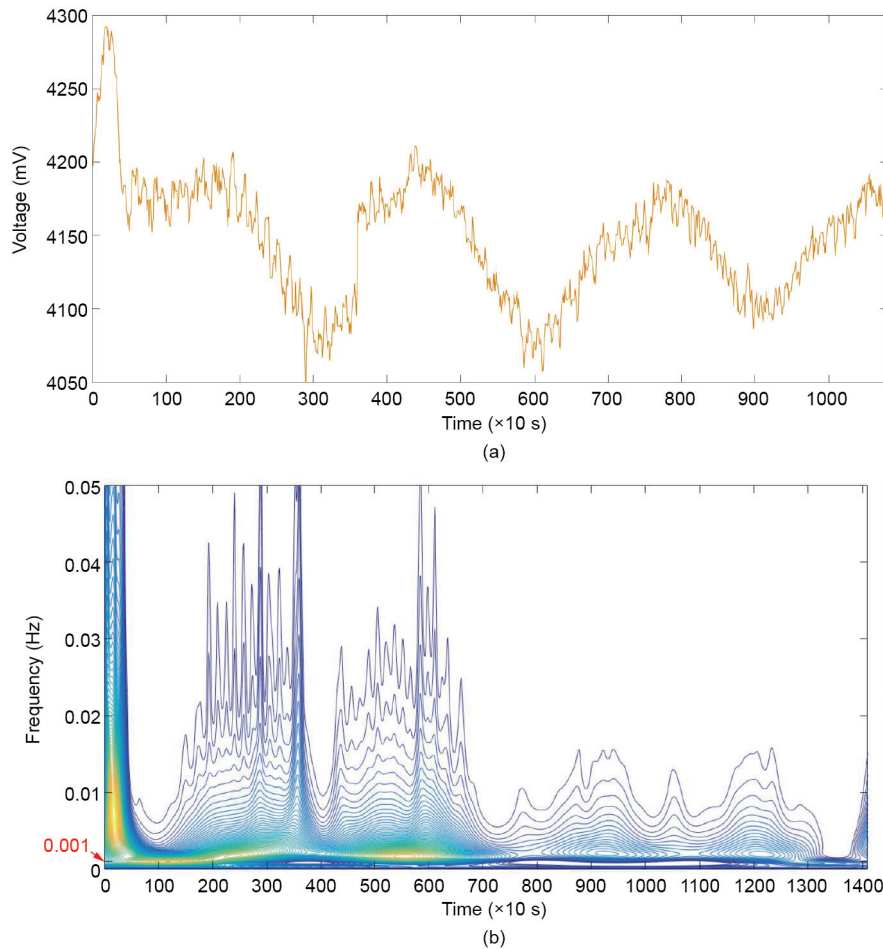
Fig. 4. Time–frequency analysis of U3 after the metal tapping operation. (a) U3; (b) scalogram of U3. The color of the color column is from dark to light, indicating the energy from weak to strong.

change in a designated frequency band with time. To compare the proposed SIEP with the EIEP, Fig. S1 in the Appendix A gives the EIEPs of each IMF obtained by the EMD of U1–U4. In Fig. S1, U1 and U3 correspond to seven IMFs, but U2 and U4 correspond to eight IMFs.

After performing the EMD, the non-stationary time series $g(t)$ is decomposed into several IMFs from high frequency to low frequency; that is, $g(t) = \sum_{i=1}^{n} c_i(t, f_i) + r_n(t)$, $f_i \in [\omega_{i,1}, \omega_{i,2}]$, $i = 1, ..., n$, where n is the number of IMF, c_i is the ith IMF, r_n is the residue, and f_i is the frequency of the ith IMF [20]. Let $H_{i,g}(t)$ be the Hilbert spectrum of the ith IMF c_i of $g(t)$; then, the EIEP of the ith IMF $E_{i,g}(t)$ is $E_{i,g}(t) = H_{i,g}^2(t)$.

To compare the EIEP and SIEP proposed in this paper, Fig. S1 gives the EIEP $E_{i,U1}(t)$, $E_{i,U2}(t)$, $E_{i,U3}(t)$, and $E_{i,U4}(t)$ of each IMF of NCVs U1–U4. It can be seen from Fig. S1 that for $E_{i,U1}(t)$ and $E_{i,U3}(t)$, $i = 1, ..., 7$; for $E_{i,U2}(t)$ and $E_{i,U4}(t)$, $i = 1, ..., 8$.

3.2. SIEP of the [0.001, 0.010] Hz band

In Fig. 6(a), $P_{U1|_{0.001}^{0.010}}(t)$ (NCD, blue), $P_{U2|_{0.001}^{0.010}}(t)$ (PAE, green), and $P_{U3|_{0.001}^{0.010}}(t)$ (AMT, yellow) are the [0.001, 0.010] Hz band SIEPs of U1, U2, and U3, respectively, which are collected under NCD, prior to the anode effect and after the metal tapping operation. The following can be seen from Fig. 6(a):

(1) When the cell condition is normal, $P_{U1|_{0.001}^{0.010}}(t)$ fluctuates gently.

(2) As the anode effect approaches, $P_{U2|_{0.001}^{0.010}}(t)$ gradually increases, which corresponds to the phenomenon in which the MPAR gradually becomes violent prior to the anode effect.

(3) With the passage of time after the completion of the metal tapping operation, $P_{U3|_{0.001}^{0.010}}(t)$ gradually decreases, which corresponds to the phenomenon in which the MPAR caused by the metal tapping operation gradually becomes steady and gentle over time.

(4) $P_{U2|_{0.001}^{0.010}}(t)$ and $P_{U3|_{0.001}^{0.010}}(t)$ are significantly greater than $P_{U1|_{0.001}^{0.010}}(t)$ and change with the severity of the MPAR: $P_{U2|_{0.001}^{0.010}}(t)$ gradually increases, starting from approximately $P_{U1|_{0.001}^{0.010}}(t)$; while $P_{U3|_{0.001}^{0.010}}(t)$ gradually decreases from being significantly greater than $P_{U1|_{0.001}^{0.010}}(t)$ to approaching $P_{U1|_{0.001}^{0.010}}(t)$.

Therefore, it can be inferred that the energy change of the NCV in [0.001, 0.010] Hz is related to the MPAR, which means that the NCV frequency band sensitive to the MPAR is within [0.001, 0.010] Hz.

Fig. S1(b) shows the EIEPs $E_{i,U2}(t)$, $i = 1, ..., 8$, arranged from high frequency to low frequency. The EIEPs are obtained by decomposing U2 into IMFs using EMD and then calculating the Hilbert energy spectrum of each IMF. The following observations can be made from Fig. S1(b): ① The EIEP5 $E_{5,U2}(t)$ calculated from IMF5 is most similar to $P_{U2|_{0.001}^{0.010}}(t)$ (PAE) in Fig. 6(a), with three obvious peaks existing, and the appearance time is closest; moreover, ② the most obvious two peak positions of EIEP4 $E_{4,U2}(t)$ calculated from IMF4 approximate the first two peak positions of $P_{U2|_{0.001}^{0.010}}(t)$ in
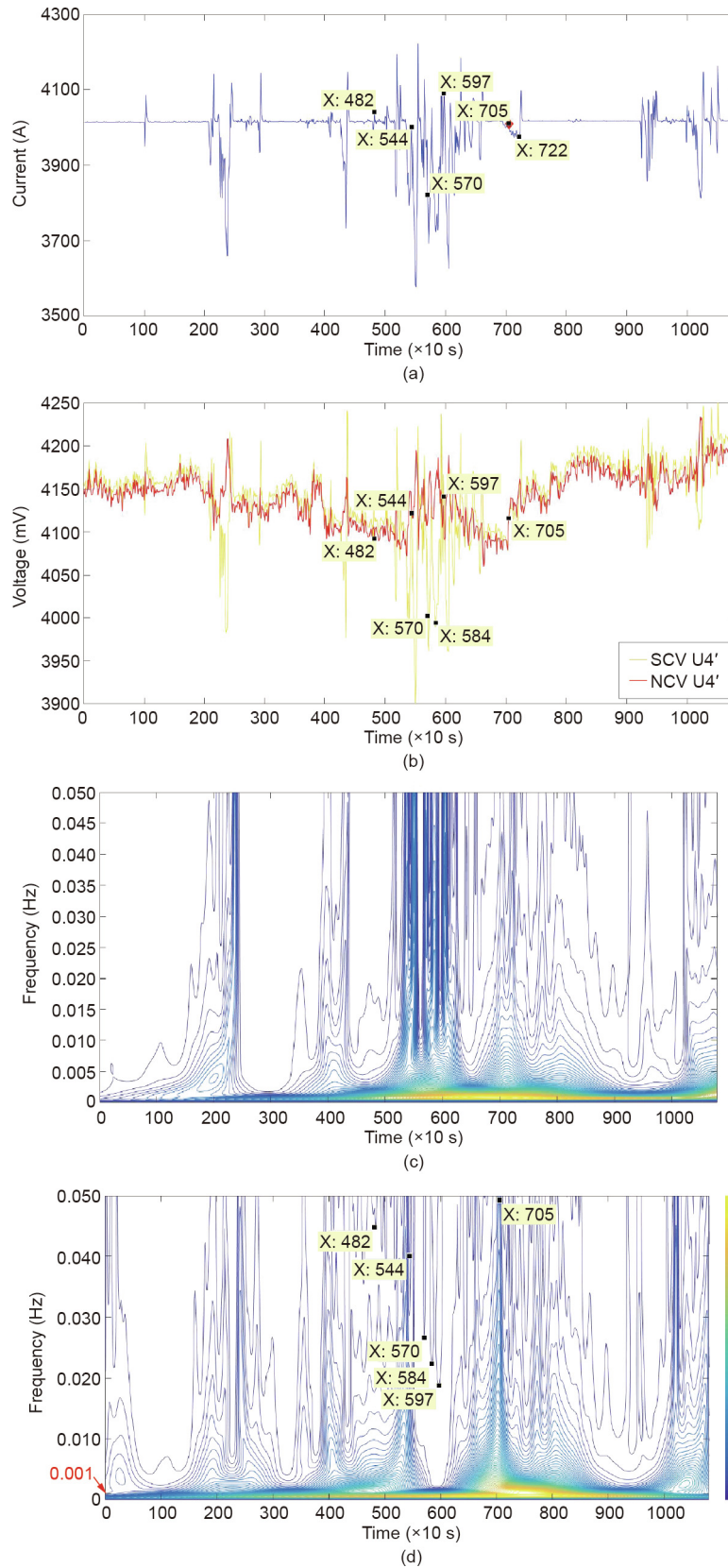
Fig. 5. NCV when the line current oscillates violently. (a) Line current I4; (b) U4 and U4′: (c) scalogram of U4′; (d) scalogram of U4. The color of the color column is from dark to light, indicating the energy from weak to strong.
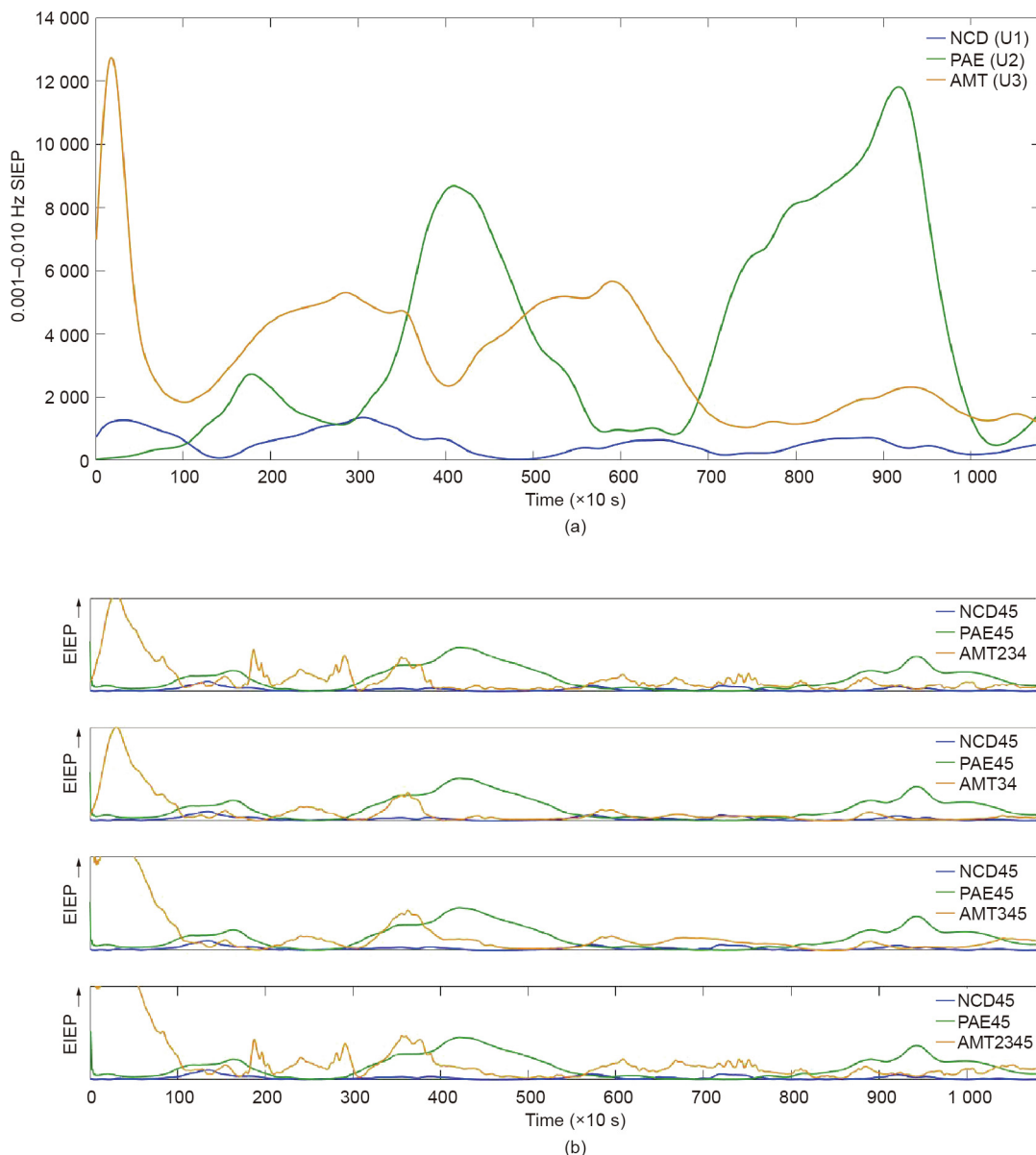
Fig. 6. [0.001, 0.010] Hz SIEPs and EIEPs of U1, U2, and U3. (a) SIEPs of the [0.001, 0.010] Hz band; (b) EIEPs.

Fig. 6(a). It can be inferred from this result that the EMD decomposes the abnormal energy information of U2 into two frequency bands corresponding to IMF4 and IMF5. Therefore, PAE45 in Fig. 6(b) is obtained by EIEP4 plus EIEP5; that is, $PAE45(t) = E_{4,U2}(t) + E_{5,U2}(t)$. As a comparison, Fig. 6(b) shows the NCD45, where $NCD45(t) = E_{4,U1}(t) + E_{5,U1}(t)$. By comparing the green curves in Figs. 6(a) and (b), it can be seen that the EIEP can basically represent the energy peaks of U2; however, it cannot reflect the increase in energy caused by the MPAR prior to the anode effect.

The following can be seen from Fig. S1(c):

(1) The most obvious peak of EIEP4 $E_{4,U3}(t)$ calculated from IMF4 approximates that of $P_{U3|_{0.001}^{0.010}}(t)$ (AMT) in Fig. 6(a).

(2) The EIEP3 $E_{3,U3}(t)$ calculated from IMF3 has obvious peaks throughout the whole sampling period, in which the peak positions in the period of 1000–4000 s approximate that of the second peak of $P_{U3|_{0.001}^{0.010}}(t)$ in Fig. 6(a). Similarly, the peak positions of EIEP3 $E_{3,U3}(t)$ in the period of 5000–7000 s in Fig. S1(c) approximate that

of the third peak of $P_{U3|_{0.001}^{0.010}}(t)$ in Fig. 6(a); in addition, the peak positions of EIEP3 $E_{3,U3}(t)$ near time 9000 s approximate that of the fourth peak of $P_{U3|_{0.001}^{0.010}}(t)$.

(3) The EIEP2 $E_{2,U3}(t)$ calculated from IMF2 also has obvious peaks in the period of 1500–3000 s, which is included in the period of the appearance time of the second peak of $P_{U3|_{0.001}^{0.010}}(t)$ in Fig. 6(a).

(4) The EIEP5 $E_{5,U3}(t)$ calculated from IMF5 also has obvious peaks at the beginning of $E_{5,U3}(t)$, corresponding to the first peak of $P_{U3|_{0.001}^{0.010}}(t)$ in Fig. 6(a).

Therefore, it can be inferred that the EMD decomposes the abnormal energy generated by the MPAR after the metal tapping operation into four frequency bands corresponding to IMF2, IMF3, IMF4, and IMF5. Thus, based on EIEP3 $E_{3,U3}(t)$ plus EIEP4 $E_{4,U3}(t)$, this paper adds EIEP2 $E_{2,U3}(t)$ and EIEP5 $E_{5,U3}(t)$ to obtain AMT234, AMT34, AMT345, and AMT2345, where

$$AMT234(t) = E_{2,U3}(t) + E_{3,U3}(t) + E_{4,U3}(t) \tag{4}$$

$$AMT34(t) = E_{3,U3}(t) + E_{4,U3}(t) \tag{5}$$

$$AMT345(t) = E_{3,U3}(t) + E_{4,U3}(t) + E_{5,U3}(t) \tag{6}$$

$$AMT2345(t) = E_{2,U3}(t) + E_{3,U3}(t) + E_{4,U3}(t) + E_{5,U3}(t) \tag{7}$$

The yellow curve in Fig. 6(b) shows that ① the EIEP represented by AMT34 fluctuates significantly before the sampling time point 4000 s; ② the EIEP represented by AMT345 fluctuates more than that of AMT34 after the sampling time point 500; and ③ the fluctuation positions of AMT2345 are basically the same as those of AMT345, but contain more details than those of AMT345. By comparing the yellow curves in Figs. 6(a) and (b), it can be seen that the EIEP represents the energy fluctuation; however, it cannot reflect the decrease in abnormal energy, which is caused by the gradual weakness of the MPAR after the metal tapping operation.

In this subsection, NCV U2 prior to the anode effect and NCV U3 after the metal tapping operation are taken as examples in order to compare in detail the effects of the SIEP and EIEP on the abnormal energy in cell voltage caused by MPAR. Compared with the EIEP,

the SIEP proposed in this paper is more accurate and detailed in decomposing the frequency bands of the NCV; in addition, it can represent the energy change in the designated frequency band [0.001, 0.010] Hz, and thus better reflects the abnormal change in the NCV energy caused by MPAR. Based on the energy change of the voltage quantitatively represented by the SIEP, it can be determined that the sensitive frequency band of the MPAR is [0.001, 0.010] Hz.

3.3. SIEP of the [0.01, 0.05] Hz band

Fig. 7(a) is a comparison of the SIEP of two cell conditions. In Fig. 7(a), the blue curve is $P_{U1|_{0.01}^{0.05}}(t)$ (NCD) under NCD; the red curve is $P_{U4|_{0.01}^{0.05}}(t)$ (CO-N) under the cell condition when the line current oscillates violently; and the yellow curve is $P_{U4'|_{0.01}^{0.05}}(t)$ (CO-S) of the sampling cell voltage under the cell condition when the line current oscillates violently. From Fig. 5(a) and Fig. 7(a), the following is known:
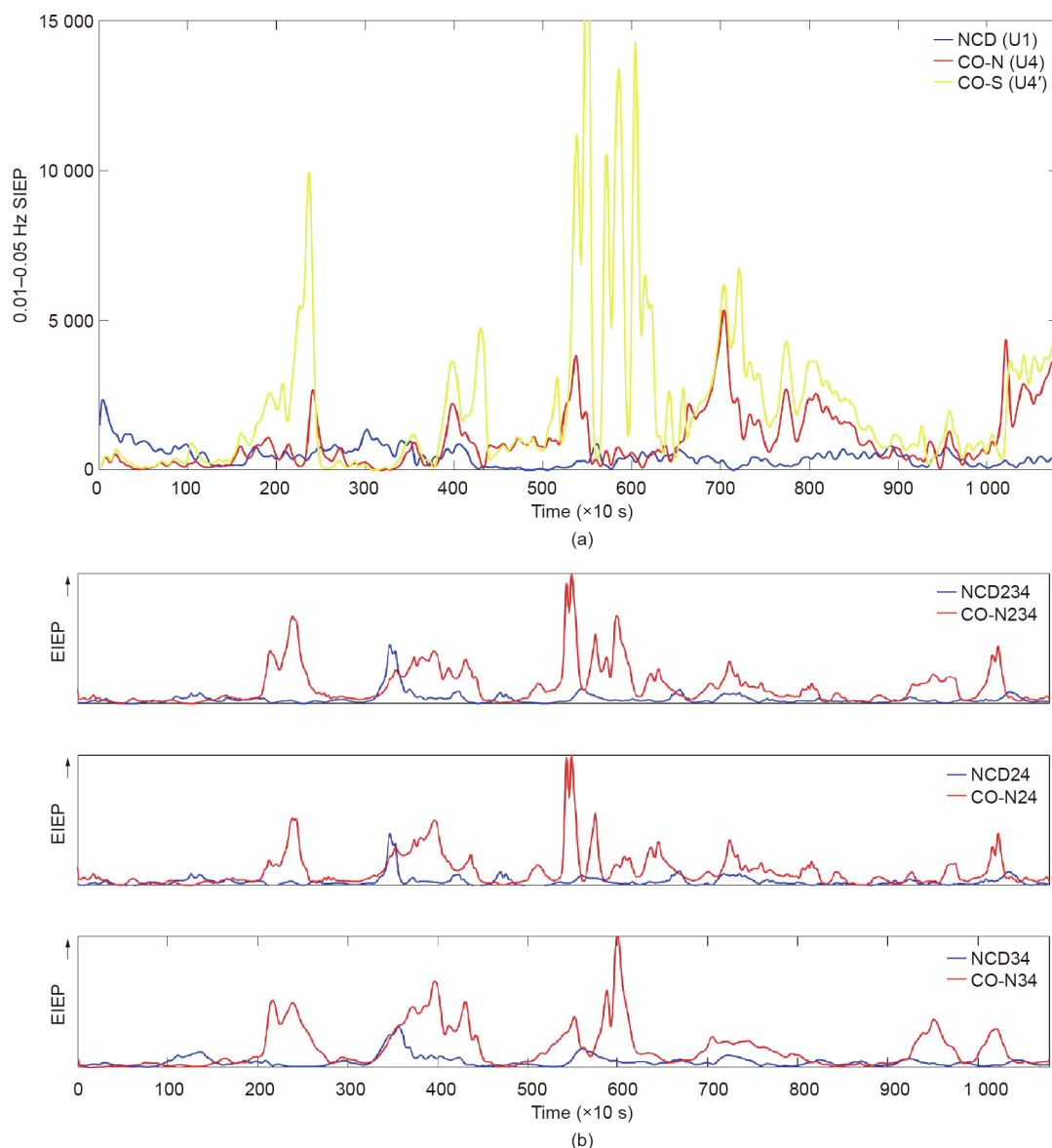

Fig. 7. Comparison of the SIEP of the [0.01, 0.05] Hz band and the EIEP when the line current oscillates violently. (a) SIEP of the [0.01, 0.05] Hz band; (b) EIEPs of U4. CO-N: the EIEP of NCV U4 when the line current oscillates violently; CO-S: the EIEP of sampling cell voltage U4′ when the line current oscillates violently.

(1) Corresponding to the sampling periods of 2000–2500, 4000–4500, and 5000–6500 s with violent COs, the SIEP $P_{U4'|_{0.01}^{0.05}}(t)$ of the sampling cell voltage also fluctuates severely.

(2) In the above sampling period with violent COs, the fluctuation of the SIEP $P_{U4|_{0.01}^{0.05}}(t)$ of the NCV is significantly flatter than that of $P_{U4|_{0.01}^{0.05}}(t)$, but there are still obvious peaks, which indicates that Eq. (2) can partially eliminate the interference from COs.

(3) Under NCD, $P_{U1|_{0.01}^{0.05}}(t)$ is generally flat throughout the observation period, with no obvious fluctuation.

Therefore, it is concluded that the energy anomaly of the NCV introduced by violent COs is mainly reflected in the frequency band above 0.01 Hz; that is, the sensitive frequency band of the NCV related to the violent COs is within [0.01, 0.05] Hz, which is consistent with the conclusions in Refs. [12,17].

From Fig. S1(d), it is known that only the EIEP4 $E_{4,U4}(t)$ calculated from IMF4 has a significant peak near the 4000–4500 s region, in which the sampling line current I4 oscillates violently in Fig. 5(a). In Fig. S1(d), EIEP2 $E_{2,U4}(t)$ and EIEP3 $E_{3,U4}(t)$ have obvious peaks around the 2000–2500 and 5000–6500 s regions, which approximate the violently oscillating positions of I4 in Fig. 5(a). Therefore, in Fig. 7(b), EIEP4 $E_{4,U4}(t)$ is used as the benchmark, adding EIEP2 $E_{2,U4}(t)$ and EIEP3 $E_{3,U4}(t)$ to obtain CO-N234, CO-N24, and CO-N34, where

$$CO\text{-}N234(t) = E_{2,U4}(t) + E_{3,U4}(t) + E_{4,U4}(t) \tag{8}$$

$$CO\text{-}N24(t) = E_{2,U4}(t) + E_{4,U4}(t) \tag{9}$$

$$CO\text{-}N34(t) = E_{3,U4}(t) + E_{4,U4}(t) \tag{10}$$

As a comparison, Fig. 7(b) shows the NCD234, NCD24, and NCD35, where

$$NCD234(t) = E_{2,U1}(t) + E_{3,U1}(t) + E_{4,U1}(t) \tag{11}$$

$$NCD24(t) = E_{2,U1}(t) + E_{4,U1}(t) \tag{12}$$

$$NCD34(t) = E_{3,U1}(t) + E_{4,U1}(t) \tag{13}$$

By comparing Figs. 6(a) and (b), it can be seen that the EIEP can also reflect the energy anomaly introduced by the violent COs in NCV U4. However, the energy anomaly regions shown by the SIEP proposed in this paper are finer. Moreover, the SIEP can demonstrate the energy change of the designated frequency band of [0.01, 0.05] Hz.

3.4. Summary of the quantitative representation of the NCV energy change

According to the results of the SIEP analysis, the frequency band of the NCV is divided into the following three sub-bands, which are sensitive to the cell conditions.

(1) The [0, 0.001] Hz band is the low-frequency region, which is related to the alumina concentration [14,17].

(2) The [0.001, 0.010] Hz band is related to the MPAR.

(3) The [0.01, 0.05] Hz band is related to the abnormal COs and is a sub-low-frequency noise range.

The low-frequency noise is related to the "voltage swing." Based on the characteristics of the cell voltage energy distribution in this frequency band, the low-frequency noise region of [0.001, 0.05] is subdivided into the [0.001, 0.010] Hz MPAR frequency band and the [0.01, 0.05] Hz sub-low-frequency noise band. The low-frequency range of this paper is [0, 0.001] Hz, which is narrower than that of Ref. [17]—that is, [0, 0.002] Hz—and thus is more conducive to the extraction of low-frequency signals. The research in this paper provides a reasonable passband for digital filter design

to obtain online cell condition information, and can provide a reliable online basis for cell condition analysis and control decisions.

By quantitative representation with the SIEP, it is concluded that the energy changes of the signal components in different frequency bands of the NCV have specific process semantemes and can describe the specific cell conditions. When the SIEP in a certain frequency band is abnormal, it indicates that the cell condition corresponding to that frequency band is also abnormal. Since the SIEP can be obtained online, and has significant characteristics under different cell conditions, it can be used as a feature of an intelligent algorithm [37,38] for online cell condition recognition, thereby providing an online basis for control decisions. In addition, the SIEP is the deep knowledge derived from the NCV and can participate in the knowledge graph construction of aluminum electrolysis in the form of conception or property [37,39], which is very helpful for acquiring implicit knowledge from the knowledge graph.

4. Conclusions

This paper combines mechanism knowledge and scalograms to conduct a qualitative analysis of the NCV under a variety of representative cell conditions and uses the proposed SIEP to acquire and quantitatively represent the energy change in the cell condition-sensitive frequency band of each cell condition. The SIEP can characterize the energy change with time in the designated frequency band of the analyzed signal. Compared with the EIEP, the SIEP can describe the energy change in any frequency band within the effective frequency band of the NCV more finely. The proposed frequency segmentation method is more sensitive to cell condition changes and is beneficial in obtaining more elaborate details of online cell condition information, thus providing a more reliable and accurate online basis for cell condition monitoring and control decisions.

This research is part of knowledge acquisition and knowledge representation in process industry knowledge automation [37,39,40]. The SIEP has process semantemes and can be obtained online; therefore, it can provide online deep knowledge for big data-driven knowledge reasoning [37,41] and other work.

Compliance with ethics guidelines

Zhaohui Zeng, Weihua Gui, Xiaofang Chen, Yongfang Xie, Hongliang Zhang, and Yubo Sun declare that they have no conflict of interest or financial conflicts to disclose.

Appendix A. Supplementary data

Supplementary data to this article can be found online at https://doi.org/10.1016/j.eng.2020.11.012.

References

[1] Blatch GI, Taylor MP, Fyfe M, inventors; Comalco Aluminum Ltd., assignee. Process for controlling aluminum smelting cells. United States Patent US 5089093. 1992 Feb 18.

[2] Simakov DA, Gusev AO, Bakin KB, inventors; United Company RUSAL Engineering and Technology LLC., assignee. Method for controlling an alumina feed to electrolytic cells for producing aluminum. United States Patent US 10472725. 2019 Nov 12.

[3] Schneller MC. *In situ* alumina feed control. JOM 2009;61(11):26–9.

[4] Schneller M, inventor. Aluminum production process control. United States Patent US 8052859. 2011 Nov 8.

[5] Zhou K, Lin Z, Yu D, Cao B, Wang ZQ, Guo S. Cell resistance slope combined with LVQ neural network for prediction of anode effect. In: Proceedings of 2015 Sixth International Conference on Intelligent Control and Information Processing (ICICIP); 2015 Nov 26–28; Wuhan, China; 2016. New York City: IEEE; 2016. p. 47–51.

[6] Meghlaoui A, inventor; Dubai Aluminium Company Ltd., assignee. Intelligent process control using predictive and pattern recognition techniques. United States Patent US 6609119. 2003 Aug 19.

[7] Thonstad J, Utigard TA, Vogt H. On the anode effect in aluminum electrolysis. In: Bearne G, Dupuis M, Tarcy G, editors. Essential readings in light metals. Cham: Springer; 2016. p. 131–8.

[8] Haurpin WE. Polarization in an aluminum reduction cell. J Electrochem Soc 1956;103(3):174–8.

[9] Bearne GP. The development of aluminum reduction cell process control. JOM 1999;51(5):16–22.

[10] Banta L, Dai C, Biedler P. Noise classification in the aluminum reduction process. In: Bearne G, Dupuis M, Tarcy G, editors. Essential readings in light metals. Cham: Springer; 2016. p. 812–6.

[11] Ding L, Zeng SP, Zeng Z. Spectral analysis of cell resistance signals in 350 kA aluminum reduction cells. Tech Autom Appl 2005;24(12):68–77. Chinese.

[12] Xiao J, Li J, Yang JH, Zou Z, Ye SL. Effect of line current fluctuation on process control of aluminium electrolysis. Mining Metall Eng 1999;19(3):44–6. Chinese.

[13] Bonny P, Gerphagnon JL, Laboure G, Keinborg M, Homsi P, Langon B, inventors; Pechiney, assignee. Process and apparatus for accurately controlling the rate of introduction and the content of alumina in an igneous electrolysis tank in the production of aluminium. United States Patent US 4431491. 1984 Feb 14.

[14] Zeng Z, Gui W, Chen X, Xie Y, Wu R. A mechanism knowledge-driven method for identifying the pseudo dissolution hysteresis coefficient in the industrial aluminium electrolysis process. Control Eng Pract 2020;102:104533.

[15] Homsi P, Peyneau JM, Reverdy M. Overview of process control in reduction cells and potlines. In: Bearne G, Dupuis M, Tarcy G, editors. Essential readings in light metals. Cham: Springer; 2016. p. 739–46.

[16] Verdenik A. Analysis and visualization of aluminum reduction cell noise based on wavelet transform. In: Williams E, editor. Light metals 2016. Cham: Springer International Publishing; 2016. p. 403–8.

[17] Li J, Liu Y, Huang Y, Wang H. Studies on the modelling of control signal filtering and noise analysis for the aluminium electrolytic process. J Cent South Inst Min Metall 1993;24(3):318–25. Chinese.

[18] Dupuis M. Cell voltage noise removal and cell voltage (or resistance) slope calculation. IFAC Proc 2007;40(11):490–2.

[19] Li M, Cui Y, Yang J, Hao D. An adaptive multi-domain fusion feature extraction with method HHT and CSSD. Acta Electron Sin 2013;41(12):2479–86. Chinese.

[20] Huang NE, Shen Z, Long SR. A new view of nonlinear water waves: the Hilbert spectrum. Annu Rev Fluid Mech 1999;31(1):417–57.

[21] Mallat S. A wavelet tour of signal processing. 3rd ed. San Diego: Academic Press; 2008. p. 11–4.

[22] Cohen L. Time–frequency distributions—a review. Proc IEEE 1989;77 (7):941–81.

[23] Qian S, Chen D. Joint time–frequency analysis. IEEE Signal Process Mag 1999;16(2):52–67.

[24] Hess-Nielsen N, Wickerhauser NMV. Wavelets and time–frequency analysis. Proc IEEE 1996;84(4):523–40.

[25] Bolós VJ, Benítez R. The wavelet scalogram in the study of time series. In: Casas E, Martínez V, editors. Advances in differential equations and applications. Cham: Springer International Publishing; 2014. p. 147–54.

[26] Tomasson GG, Melville WK. Geostrophic adjustment in a channel: nonlinear and dispersive effects. J Fluid Mech 1992;241:23–57.

[27] Urata N. Wave mode coupling and instability in the internal wave in aluminum reduction cells. In: Bearne G, Dupuis M, Tarcy G, editors. Essential readings in light metals. Cham: Springer; 2016. p. 373–8.

[28] Chiampi M, Repetto M, Chechurin V, Kalimov A, Leboucher L. Magnetic modeling and magneto–hydro–dynamic simulation of an aluminum production electrolytic cell. Compel Int J Comp Math Electr Electron Eng 1999;18(3):528–38.

[29] Xu Y, Li J, Zhang H, Lai Y. MHD calculation for aluminium electrolysis based on nonlinear shallow water model. Chin J Nonferrous Met 2011;21(1):191–7. Chinese.

[30] Wang Z, Feng N, Peng J, Wang Y, Qi X. Study of surface oscillation of liquid aluminum in 168 kA aluminum reduction cells with a new type of cathode design. In: Johnson JA, editor. Light metals 2010. Seattle: The Minerals, Metals & Materials Society; 2010. p. 485–8.

[31] Wang Y, Tie J, Tu G, Sun, Zhao R, Zhang Z. Effect of gas bubble on cell voltage oscillations based on equivalent circuit simulation in aluminum electrolysis cell. Trans Nonferrous Met Soc China 2015;25(1):335–44.

[32] Shen X. The mechanism of voltage fluctuation in aluminum reduction cell and its precautions. Light Met 2008;9:31–5. Chinese.

[33] Haupin WE. A scanning reference electrode for voltage contours in aluminum smelting cells. JOM 1971;23(10):46–9.

[34] Zhao ZB. [High temperature experimental study and numerical simulation of bubble dynamics in aluminum electrolytic process] [dissertation]. Shenyang: Northeastern University School of Metallurgy; 2016. Chinese.

[35] Li J, Tu G, Qi X, Mao J, Lu D, Feng N. Real-time monitoring and analysis on fluctuation state of liquid aluminum in 300 kA and 400 kA aluminum reduction cell. Light Met 2012;2:30–9. Chinese.

[36] Yang Z. [Causes and treatment measures of voltage pendulum in 300 kA aluminum electrolytic cell]. Technol Enterp 2012;20:289–91. Chinese.

[37] Mao S, Wang B, Tang Y, Qian F. Opportunities and challenges of artificial intelligence for green manufacturing in the process industry. Engineering 2019;5(6):995–1002.

[38] Chen H, Jiang B, Lu N. An improved incipient fault detection method based on Kullback–Leibler divergence. ISA Trans 2018;79:127–36.

[39] Gui W, Chen X, Yang C, Xie Y. Knowledge automation and its industrial application. Sci Sin Inform 2016;46(8):1016–34. Chinese.

[40] Cai T. Industrial process control systems: research status and development direction. Sci Sin Inform 2016;46(8):1003–15. Chinese.

[41] Chen H, Jiang B, Ding SX, Lu N, Chen W. Probability-relevant incipient fault detection and diagnosis methodology with applications to electric drive systems. IEEE Trans Control Syst Technol 2019;27(6):2766–73.